

Article

Argon Adsorption on Cationic Gold Clusters Au_n^+ ($n \leq 20$)

Piero Ferrari  and Ewald Janssens * 

Quantum Solid-State Physics, Department of Physics and Astronomy, KU Leuven, 3001 Leuven, Belgium; piero.ferrari@kuleuven.be

* Correspondence: ewald.janssens@kuleuven.be

Abstract: The interaction of Au_n^+ ($n \leq 20$) clusters with Ar is investigated by combining mass spectrometric experiments and density functional theory calculations. We show that the inert Ar atom forms relatively strong bonds with Au_n^+ . The strength of the bond strongly varies with the cluster size and is governed by a fine interplay between geometry and electronic structure. The chemical bond between Au_n^+ and Ar involves electron transfer from Ar to Au, and a stronger interaction is found when the Au adsorption site has a higher positive partial charge, which depends on the cluster geometry. Au_{15}^+ is a peculiar cluster size, which stands out for its much stronger interaction with Ar than its neighbors, signaled by a higher abundance in mass spectra and a larger Ar adsorption energy. This is shown to be a consequence of a low-coordinated Au adsorption site in Au_{15}^+ , which possesses a large positive partial charge.

Keywords: gold clusters; argon; adsorption energies; mass spectrometry; density functional theory



Citation: Ferrari, P.; Janssens, E. Argon Adsorption on Cationic Gold Clusters Au_n^+ ($n \leq 20$). *Molecules* **2021**, *26*, 4082. <https://doi.org/10.3390/molecules26134082>

Academic Editors: Marco Baron, Cristina Tubaro and Andrea Biffis

Received: 10 June 2021

Accepted: 1 July 2021

Published: 4 July 2021

Publisher's Note: MDPI stays neutral with regard to jurisdictional claims in published maps and institutional affiliations.



Copyright: © 2021 by the authors. Licensee MDPI, Basel, Switzerland. This article is an open access article distributed under the terms and conditions of the Creative Commons Attribution (CC BY) license (<https://creativecommons.org/licenses/by/4.0/>).

1. Introduction

As a bulk material, gold is the noblest of all metals [1]. At the nanoscale, however, gold becomes reactive towards several molecules, and can selectively catalyze certain reactions, which has attracted broad scientific attention [2–5]. Intriguingly, gold cationic clusters are also reactive towards noble gas atoms [6]. The inertness of noble gases was challenged by the work of P. Pyykkö, who in 1995 proposed that the bond between Au^+ ions with different noble gases (Ng = Ar, Kr, Xe) has a partially covalent character, and cannot merely be ascribed to the expected weak dispersion forces [7]. While this claim was controversial at that time [8–10], it is nowadays accepted, and noble gas chemistry has become an active research field, with Au-based systems drawing significant attention [6,11].

The properties of gold clusters differ significantly from those of copper and silver coinage metal clusters [12–15]. The intriguing properties of gold clusters are not restricted to their reactivity, but also to unique ground-state geometries [16], optical absorption [17], relative stability [18] and radiative cooling [19], and are largely related to the relativistic nature of the Au atom [20]. One consequence of the relativistic effects in Au is an enhanced electron affinity [20], if compared, for instance, with Ag and Cu. The high electron affinity was shown to favor electron transfer from the Ng atom to Au in the $AuNg^+$ dimer and therefore the formation of a relatively strong bond [21].

Using the Au_3^+ trimer as a model system, the interaction between Au and Ar was investigated by Fielicke and collaborators, using a combination of infrared spectroscopy and density functional theory (DFT) calculations [22]. Ar was shown to be heavily involved in the highest frequency vibrational modes of $Au_3Ar_m^+$ complexes, something that was attributed to a relativistically enhanced covalency of the Au-Ar interaction. This conclusion was supported by performing experiments on $Ag_{3-n}Au_n^+$ clusters, where the Ar bonding decreased with increasing silver concentration. Subsequent work by the same authors demonstrated similar characteristics of the interaction of Ar with Au_4^+ and Au_5^+ , namely, electron transfer from Ar to the cationic gold clusters and the formation of a strong bond of partial covalent character [23].

The attachment of Ar (and other noble gas elements) to larger cationic gold clusters has been reported. For example, Ar has been used as a tagging/spectator atom when investigating the geometries and the optical absorption spectra of pure and doped gold clusters [24–28]. Moreover, in investigations of the optical absorption of Au_n^+ clusters in the $n = 13$ –20 size range, Xe was employed as the tagging element instead of Ar, as the interaction of the latter noble gas element was seen to decrease with cluster size and therefore, it was easier to form the complexes with Xe [29]. Nevertheless, the nature of the interaction between the noble gas atoms with Au_n^+ , in a broad size range, has not been explained. For instance, Au_{15}^+ has been noticed to adsorb a larger amount of Ar than the closest size neighbors [28]. This feature is unexpected, as Au_{15}^+ possesses a closed electronic configuration, and therefore, might be expected to be less reactive than the open-shell neighboring sizes.

In this work, we address the interaction between Au_n^+ clusters with Ar, by performing density functional theory calculations in the extended $n \leq 20$ size range, in combination with mass spectrometric experiments. We demonstrate the formation of a (partial) chemical bond between Ar and the clusters, which is a consequence of an electron charge donation from Ar to Au. The strength of the cluster–argon interaction is strongly size dependent, and is well correlated with the geometry of the Au_n^+ clusters.

2. Methods

2.1. Experimental

The gold clusters were produced with the laser ablation technique [30], in a setup that is described in detail in Reference [31]. In short, a bulk gold plate was ablated by a tightly focused nanosecond Nd:YAG laser (second harmonic, 532 nm), and the generated plasma was cooled by a pulse of ultrapure He gas, added into the cluster source at a pressure of 8 bar. The mixture gold-He expands supersonically into vacuum, generating a molecular beam that was collimated by a 1 mm skimmer and was analyzed by reflectron time-of-flight mass spectrometry ($\Delta m/m \approx 1000$). The laser power density and the time delay between the gas injection and the ablation were optimized to produce Au_n^+ clusters in the $n \leq 20$ size range. Neutral and anionic species were also formed by this technique, however, they were not detectable by the mass spectrometer in the current settings. In order to make argon complexes, the He gas was mixed with 2% of Ar and the source was cooled to 250 K, resulting in $Au_nAr_m^+$ complexes with up to $m = 5$, depending on cluster size. If a lower source temperature is used, the clusters are covered with even more Ar, whereas the amount of Ar attachment was minor for the larger clusters at higher source temperatures.

2.2. Computational

Density functional theory calculations were performed to complement the mass spectrometric findings, covering the entire range of $Au_nAr_m^+$ clusters with $n = 3$ –20 and $m \leq 5$. All calculations were conducted employing the ORCA 4.2.1 software package [32], by using the PBE exchange-correlation functional [33], in conjunction with the Def2-TZVPP basis set [34]. The Stuttgart Def2-ECP pseudopotential was employed for Au, which treats explicitly 19 valence electrons [34]. Scalar relativistic effects are included in the ECP. All the electrons of Ar were considered in the calculations. Dispersion forces were accounted for via the D3BJ dispersion-correction [35]. This level of theory was shown to be accurate and computationally efficient for describing the interactions in Au^+Ar_m ($m \leq 4$) [21]. The geometries of the bare Au_n^+ ($n = 3$ –20) clusters were adopted from previous works. Infrared multiple photon dissociation spectroscopy was used in conjunction with DFT calculations to determine the geometries of the $n = 3$ –9 sizes in Reference [24], whereas an extensive global search of low-energy isomers was performed for the bare clusters up to $n = 20$ in Reference [36]. Here, we have adopted the bare cluster geometries determined in Reference [24] up to $n = 9$, and those from Reference [36] in the $n = 10$ –20 size range. We note that in Reference [24], the same level of theory as applied here was selected and a benchmark analysis showed that it accurately describes the vibrational modes of $Au_nAr_m^+$

clusters. To locate the preferred Ar adsorption sites, Ar was then placed at all possible atop coordination positions, followed by geometry optimization. Starting geometries with other Ar coordination sites were tested as well. Nevertheless, atop adsorption sites always resulted in lower total energies.

The adsorption energy (E_{ads}) of the m th attached Ar atom in the $Au_nAr_m^+$ complex was calculated by Equation (1):

$$E_{ads}(n, m) = E(Au_nAr_m^+) - E(Au_nAr_{m-1}^+) - E(Ar) \quad (1)$$

where E is the (absolute) total energy of the cluster in parenthesis. The reported adsorption energies have not been corrected for zero point energy. Moreover, Wiberg bond indexes and electron localization functions (ELF) have been calculated using the Multiwfn software package [37].

3. Results

The mass spectrometric results are summarized in Figure 1, where the fractional distribution of Ar in the $Au_nAr_m^+$ cluster is presented. These fractions are defined by Equation (2), with I the area of the peak corresponding to the complex within parenthesis in the mass spectrum.

$$F_n(m) = \frac{I(Au_nAr_m^+)}{\sum_i I(Au_nAr_i^+)} \quad (2)$$

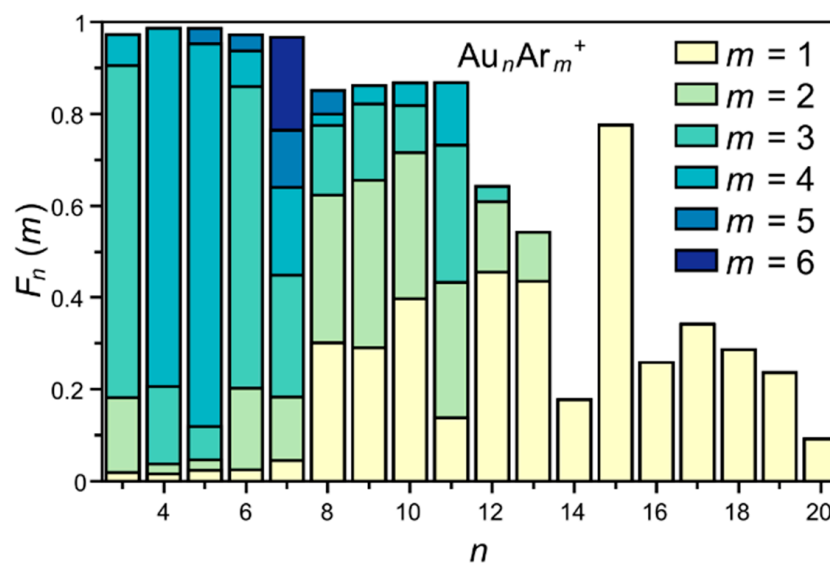


Figure 1. Fractional distribution of adsorbed Ar atoms in $Au_nAr_m^+$ ($n = 3-20$, $m = 1-6$) clusters, plotted as a stacked bar chart.

There are several interesting observations from Figure 1. (i) First of all, more Ar adsorbs on the smaller cationic clusters. More specifically, up to $n = 7$, the intensity of bare Au_n^+ is very small, (i.e., the difference between 1 and the stacked bar chart of the argon fractions for $m = 1-5$ and $n = 3-6$, and for $m = 1-6$ and $n = 7$) as is the fraction of the complexes with a single Ar atom, $m = 1$. (ii) Second, for these smaller clusters ($n \leq 7$), the $F_n(m)$ fractions with $m = 2-5$ are strongly size-dependent. Au_3^+ and Au_6^+ mainly adsorb three Ar atoms, while Au_4^+ and Au_5^+ primarily attach four. For Au_7^+ , the $F_7(m)$ fractions with $m = 2, 3, 4, 5$ and 6 have about the same magnitude. (iii) Au_{11}^+ adsorbs more Ar atoms than its neighboring sizes and there is a gradual decrease in Ar fraction from $n = 11$ onwards. (iv) From $n \geq 14$ onwards, only a single Ar atom is adsorbed on the clusters. (v) Last, the cluster $n = 15$ stands for its very high fraction of a single Ar atom.

In order to rationalize those mass spectrometric results, DFT calculations were performed on the $Au_nAr_m^+$ ($n = 3-20$; $m \leq 5$) clusters. The geometries of the complexes

that have a single Ar atom adsorbed are depicted in Figure 2. In all cases, Ar adopts an atop coordination in the lowest-energy configuration, and its presence hardly affects the geometries of the bare Au_n^+ clusters [24,36]. The possibility that isomers with a different adsorption site for Ar are present in the molecular beam, or that there is fluxionality between different adsorption sites, cannot be excluded [27]. As an example, isomers with a different Ar adsorption site for Au_4Ar^+ and Au_6Ar^+ are presented in the supporting information. The relative energies of these isomers are high enough to assume that they will not be present in large amounts in the molecular beam, however this cannot be excluded for other sizes. The results provided in the following support our analysis only considering the lowest energy configurations.

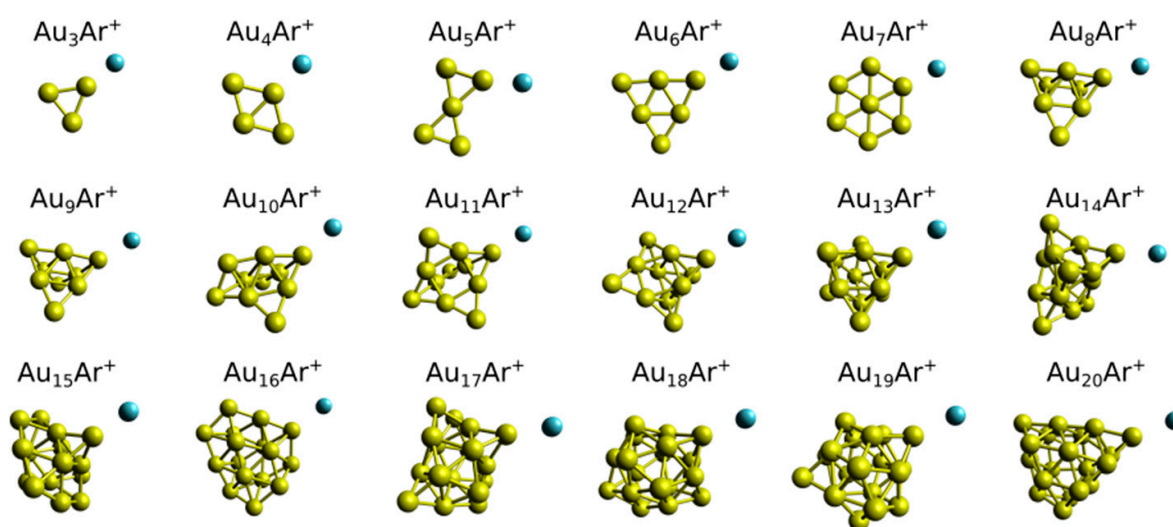


Figure 2. Optimized geometries of Au_nAr^+ ($n = 3$ – 20) clusters, calculated at the PBE+D3/ECP(def2-TZVPP) level.

For the single Ar lowest energy isomers up to $n = 7$ the Au framework is planar; for all larger sizes the metal frameworks are three-dimensional. Therefore, a first correspondence between the Au_n^+ cluster geometries and the experimental Ar fractions is already identified, namely the amount of adsorbed Ar decreases sharply at the transition size from planar to three-dimensional clusters, i.e., after Au_7^+ . A similar effect was seen in anionic Au_n^- species, where the size-dependent attachment of Ar was found to decrease abruptly once the clusters were three-dimensional [26]. The particular geometry adopted by the Au_{15}^+ cluster may also provide a hint for the higher $F_{15}(1)$ fraction. It is formed by a double layer of atoms, with a Au atom located on one layer [38]. As shown in Figure 2, this low-coordinated Au atom in Au_{15}^+ is the adsorption site of the first Ar.

The observation that Ar adsorbs on atop coordination sites in the Au_n^+ clusters may help in understanding the size-dependent Ar fractions in the $n \leq 7$ size range. Indeed the triangular shape of the Au_3^+ cluster with three equivalent atop adsorption sites is consistent with the large $F_3(3)$ fraction. Similarly, the rhombic geometry of Au_4^+ has four possible atop sites for Ar adsorption, and the higher fraction for this size is $F_4(4)$. Au_5^+ has a bowtie-like geometry with four equivalent low-coordinated sites, consistent with the observed high $F_5(4)$ fraction. The triangular shape of Au_6^+ has three corners on which atop Ar adsorption is possible, and $F_6(3)$ is the largest fraction (a second isomer of Au_6^+ has been seen in Reference [24] from which a similar conclusion can be drawn, as it also has three corners). Finally, Au_7^+ has a hexagonal shape with a Au atom at its center, hence six equivalent adsorption sites. In this cluster, similar fractions are observed for 2, 3, 4, 5 and 6 Ar atoms (it is the only cluster for which we find an m value as high as 6). Some examples of geometries for Au_n^+ clusters with multiple attached Ar atoms are presented in Figure 3 (all $m = 0$ – 5 structures are available as Supplementary Materials). We remark that the discussion of Ar fractions in relation to the Au_n^+ cluster geometries is illustrative,

but that further analysis of energetics as well as electronic structures are required to better understand the features observed experimentally.

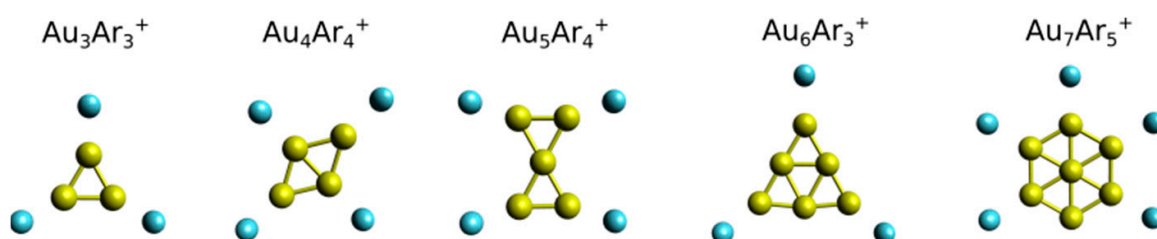


Figure 3. Optimized geometries of a selection of $Au_n Ar_m^+$ ($n = 3-7$) clusters with multiple Ar atoms attached.

Using Equation (1), the adsorption energies (E_{ads}) of the m th adsorbed Ar atom in $Au_n Ar_m^+$ were calculated. For this, the optimized geometries of the $Au_n Ar_m^+$ clusters were employed, which are shown in Figure 2 for $m = 1$ (some complexes with larger m are presented in Figure 3 and the others are available as Supplementary Materials). The obtained E_{ads} energies are given in Figure 4. Several, if not all, experimental observations about the Ar fractions can be understood based on these adsorption energies. (a) The adsorption energies show an overall decrease with Au_n^+ size, in agreement with the Ar fractions being higher for the smaller clusters. (b) For $n = 3$, there is a sudden decrease in E_{ads} at $m = 4$, while for $n = 4$ and 5, the values remain high up to $m = 4$. For $n = 6$, E_{ads} is low for $m = 4$, while for $n = 7$, the energies are relatively high up to $m = 6$ (for $m = 6$, E_{ads} is 0.16 eV). (c) There are local maxima in E_{ads} for $m = 1$ at $n = 11$ and $n = 15$. (d) The adsorption energies slightly increase around $n = 17$, decreasing again at $n = 19$. Hence, the DFT calculations reproduce outstandingly well the mass spectrometric observations.

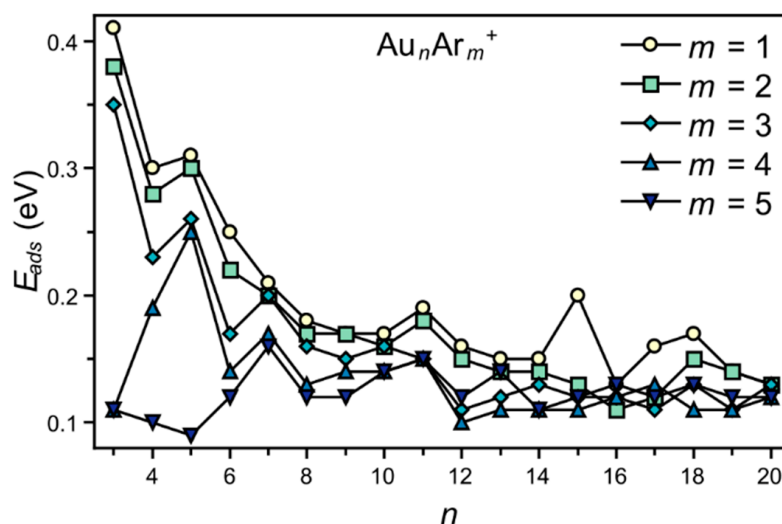


Figure 4. Adsorption energies of the m th adsorbed Ar atom in the $Au_n Ar_m^+$ clusters, calculated using Equation (1).

4. Analysis

The Hirshfeld partial charge at the Au adsorption site in bare Au_n^+ and that of Ar in $Au_n Ar^+$ are presented in panel (a) of Figure 5. Qualitatively similar results were obtained with Löwdin partial charges analysis, but are not further discussed. The positive partial charge of the reactive Au site is +0.33 e for Au_3^+ and shows an overall decrease with size n , which is not surprising since with increasing size the total +1 charge of the cluster is distributed over more atoms. The decrease, however, is not homogeneous. In particular, the higher partial charge of the Ar adsorption site of Au_{15}^+ stands out as well as the pronounced minimum of Au_{16}^+ . Clearly, there is a strong correlation between the charge

of the gold adsorption site before Ar adsorption with that of Ar after adsorption: the adsorbed Ar is more positively charged if the adsorption site had a larger positive charge. The correlation between the Hirshfeld partial charges and E_{ads} (and therefore with the experimental results) is also clear, with an overall decrease with size and local maxima for Au_5^+ , Au_{11}^+ and particularly Au_{15}^+ . Therefore, the interaction between Au_n^+ and Ar involves the transfer of electrons from Ar to Au, a more favorable process if the adsorption site has a higher positive charge.

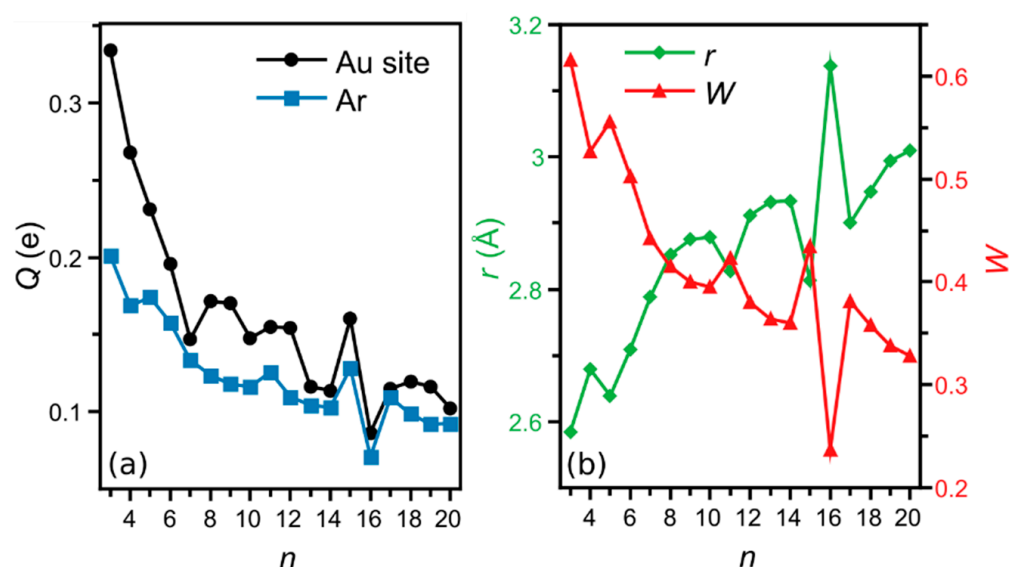


Figure 5. (a) Hirshfeld partial charge of the Au adsorption site of the bare Au_n^+ cluster (black circle), and Ar (blue square) in the $Au_n Ar^+$ complex. (b) Bond length (r —green diamonds) and Wiberg index (W —red triangles) of the Au_n-Ar^+ bond as a function of the cluster size n .

The bonding between Au_n^+ and Ar is further analyzed by calculating the Wiberg index (W) of the Au_n^+-Ar bond (structures in Figure 2), as presented in panel (b) of Figure 5. In line with the amount of electron charge from Ar to Au, the W index shows an overall decrease with n . For the smallest $n = 3, 4$ and 5 sizes the index is above 0.5, in line with the high Ar adsorption energies (above 0.3 eV). Interestingly, the Wiberg index has local maxima at Au_{11}^+ and Au_{15}^+ and a pronounced minimum at Au_{16}^+ . The correlation between the partial positive charge of Ar and the Wiberg indices, together with the W values themselves being relatively large, in particular for $n \leq 5$, reflects the formation of a chemical bond between Au_n^+ and Ar with a partial covalent character. A higher W index correlates perfectly with a smaller bond distance between Au and Ar in $Au_n Ar^+$, as shown in Figure 5b.

The density of states (DOS) of three selected clusters are presented in Figure 6: $Au_3 Ar^+$, $Au_{15} Ar^+$ and $Au_{16} Ar^+$. In each case, the DOS was projected onto the states of the Au adsorption site and of Ar. For $Au_3 Ar^+$, shown in the upper panel, there were three occupied states of major Ar character, which were highly hybridized with the states of the Au adsorption site (-16.4 , -15.3 and -14.8 eV). Such overlap between the Ar and Au states clearly indicates the formation of a formal chemical bond between the atoms, in line with the high W index (0.62) for this cluster. Similar states were found in the PDOS of $Au_{15} Ar^+$ (middle panel), however in this case, the hybridization was smaller, as highlighted by the smaller W index (0.44). In contrast, the hybridization between Au and Ar is minor in $Au_{16} Ar^+$, in correspondence with the close to zero W index in this case, being only 0.24. Such a small W index is a consequence of the very limited electron charge transfer from Ar to Au in $Au_{16} Ar^+$, as seen from Figure 5a.

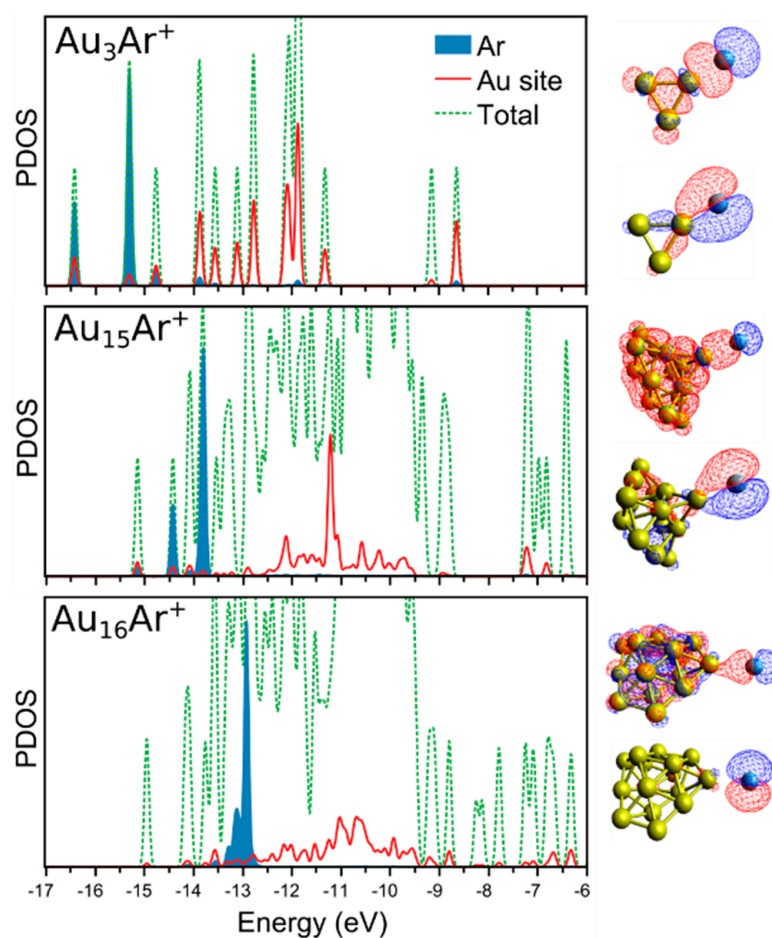


Figure 6. Density of states (DOS) of Au_3Ar^+ , $\text{Au}_{15}\text{Ar}^+$ and $\text{Au}_{16}\text{Ar}^+$ clusters. The total DOS is presented by the dotted green lines, whereas the DOS projected (PDOS) onto the states of the Au adsorption site and the Ar atom are shown by the red lines and filled blue curves, respectively. At the right, plots of two selected Kohn–Sham molecular orbitals with major contribution from Ar are presented for each cluster. These orbitals are located at energies of -16.4 and -15.3 eV for Au_3Ar^+ , -15.1 and -14.4 eV for $\text{Au}_{15}\text{Ar}^+$, and -13.1 and -12.9 eV for $\text{Au}_{16}\text{Ar}^+$, in the corresponding PDOS.

The level of hybridization between the states of Au and Ar in the PDOS of Figure 6 are quantified by the Kullback–Leibler (D_{KL}) divergence. The D_{KL} divergence is a measure of how one distribution ($p(x)$) differs from another (reference) distribution ($q(x)$), and is defined as

$$D_{KL}(p \parallel q) = \int_{-\infty}^{\infty} p(x) \ln\left(\frac{p(x)}{q(x)}\right) dx \quad (3)$$

The Kullback–Leibler divergence is zero when both distributions are identical, and increases the more they diverge from each other [39]. Using this analysis to quantify the hybridization between Au and Ar gives the values 3.18, 3.40 and 3.51, for Au_3Ar^+ , $\text{Au}_{15}\text{Ar}^+$ and $\text{Au}_{16}\text{Ar}^+$, respectively. Therefore, the overlap between Au and Ar is larger in Au_3Ar^+ , as expected, given its very high Ar adsorption energy, and the larger abundance in mass spectra. The overlap is smaller in $\text{Au}_{15}\text{Ar}^+$, but is still larger than in $\text{Au}_{16}\text{Ar}^+$.

Hence, our analysis clearly shows the formation of a chemical bond between Au_n^+ and Ar. Such a bond, of significant covalent character, is strong for $n \leq 5$, and presents an overall decrease with size. $\text{Au}_{11}\text{Ar}^+$ and particularly $\text{Au}_{15}\text{Ar}^+$ stand out in this trend. Au_{15}^+ adopts a geometry with a low-coordinated Au atom that possesses a high partial positive charge, favoring electron donation from Ar, thus enhancing the Au_{15}^+ -Ar bonding. To the right of Figure 6, two molecular orbitals of Au_3Ar^+ (-16.4 and -15.3 eV orbitals),

$\text{Au}_{15}\text{Ar}^+$ (-15.1 and -14.4 eV orbitals) and $\text{Au}_{16}\text{Ar}^+$ (-13.1 and -12.9 eV orbitals) are plotted. These orbitals clearly show the strong involvement of Ar in the wavefunctions of the Au_3Ar^+ and $\text{Au}_{15}\text{Ar}^+$ clusters, an atom that therefore cannot be considered inert when interacting with these Au_n^+ clusters. The involvement of Ar in the wavefunction of $\text{Au}_{16}\text{Ar}^+$ is much smaller. The binding analysis is complemented by calculations of the electron localization function (ELF), which corresponds to the probability of finding two electrons of the same spin in a determined region of space, and is therefore a useful quantity to differentiate between chemical and physical bonds. Calculations have shown ELF values above 0.1 in between atoms interacting covalently [40]. The analysis is presented in Figure 7 for Au_3Ar^+ , $\text{Au}_{15}\text{Ar}^+$ and $\text{Au}_{16}\text{Ar}^+$, and reveals a relatively high ELF value between Au_3^+ and Ar, of 0.115. The ELF values decrease with size, being 0.086 and 0.056 for $\text{Au}_{15}\text{Ar}^+$ and $\text{Au}_{16}\text{Ar}^+$, respectively.

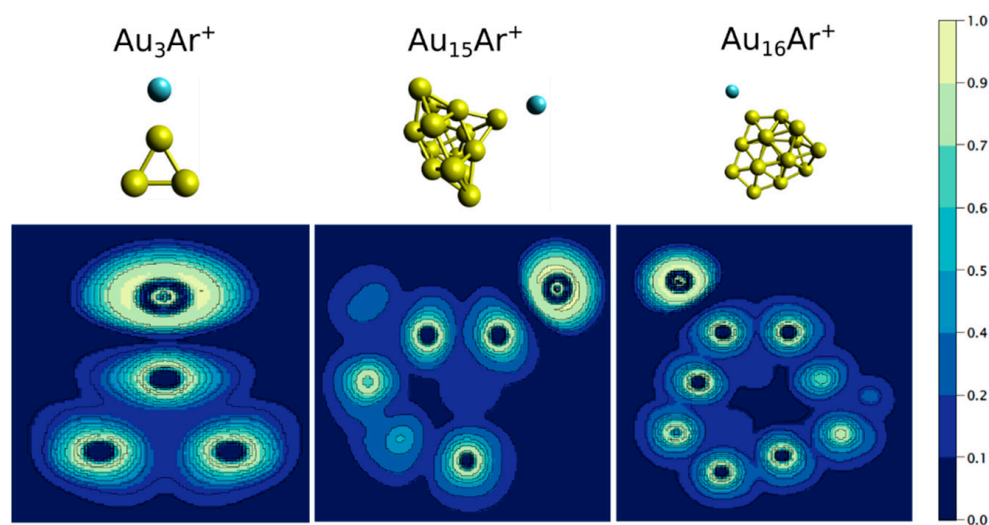


Figure 7. Electron localization function (ELF) of Au_3Ar^+ , $\text{Au}_{15}\text{Ar}^+$ and $\text{Au}_{16}\text{Ar}^+$. At the top of each panel, the geometry of the cluster is presented.

5. Conclusions

In this work, the interaction of Ar with Au_n^+ clusters was investigated in the large $n \leq 20$ size range, using a combination of mass spectrometry and density functional theory calculations. The abundances in mass spectra reveal a high propensity of the smaller clusters to form stable Au_nAr_m^+ complexes. In particular, large Ar fractions are seen in the $n \leq 7$ range. With increasing cluster size, the fraction of adsorbed Ar decreases, and above $n = 11$, only complexes with a single Ar atom are formed. In this size range, Au_{15}^+ stands out with a very high fraction of Ar. The calculations reproduce outstandingly well the mass spectrometric observations. The formation of a chemical bond between Au and Ar is proven for the investigated complexes, and is shown to be a consequence of both the geometry adopted by Au_n^+ and their electronic structure.

Supplementary Materials: The following are available online. Figure S1: Ar adsorption site isomers of Au_4Ar^+ and Au_6Ar^+ ; Figures S2–S19: Optimized geometries of Au_nAr_m^+ ($n = 3–20$; $m = 1–5$).

Author Contributions: P.F. conducted the mass spectrometric experiments and the density functional theory calculations. P.F. and E.J. performed the analysis of results, the data interpretation as well as the manuscript writing. All authors have read and agreed to the published version of the manuscript.

Funding: This research has been funded by the Research Foundation—Flanders (FWO, project G0A05.19N) and by the KU Leuven Research Council (project C14/18/073). P.F. is grateful to the FWO for a Senior Postdoctoral Fellowship. The resources and services used for the computations in this work were provided by the VSC (Flemish Supercomputer Center), funded by the FWO and the Flemish Government.

Institutional Review Board Statement: Not applicable.

Informed Consent Statement: Not applicable.

Data Availability Statement: The coordinates of the optimized $Au_nAr_m^+$ ($n = 3-20$ and $m \leq 5$) isomers are available through Github at https://github.com/pferrari13/Au_nAr_m-XYZ-coordinates.git.

Conflicts of Interest: The authors declare no conflict of interest.

Sample Availability: Not available.

References

1. Hammer, B.; Norskov, J.K. Why gold is the noblest of all the metals. *Nature* **1995**, *376*, 238–240. [CrossRef]
2. Wallace, T.W.; Whetten, R.L. Coadsorption of CO and O₂ on Selected Gold Clusters: Evidence for Efficient Room-Temperature CO₂ Generation. *J. Am. Chem. Soc.* **2002**, *124*, 7499–7505. [CrossRef]
3. Janssens, E.; Le, H.T.; Lievens, P. Adsorption of propene on neutral gold clusters in the gas phase. *Chem. Eur. J.* **2015**, *21*, 15256–15262. [CrossRef] [PubMed]
4. Abdulhussein, H.A.; Ferrari, P.; Vanbuel, J.; Heard, C.; Fielicke, A.; Lievens, P.; Janssens, E.; Johnston, R.L. Altering CO binding on gold cluster cations by Pd-doping. *Nanoscale* **2019**, *11*, 16130–16141. [CrossRef]
5. Lang, S.M.; Bernhardt, T.M.C.V.; Bakker, J.M.; Barnett, R.N.L.U. Selective C–H bond cleavage in methane by small gold clusters. *Angew. Chem. Int. Ed.* **2017**, *56*, 13406–13410. [CrossRef]
6. Pan, S.; Jana, G.; Merino, B.; Chattaraj, P.K. Noble-noble strong union: Gold at its best to make a bond with a noble gas atom. *ChemistryOpen* **2019**, *8*, 173–187. [CrossRef]
7. Pyykko, P. Predicted chemical bonds between rare gases and Au⁺. *J. Am. Chem. Soc.* **1995**, *117*, 2067–2070. [CrossRef]
8. Read, J.P.; Buckingham, A.D. Covalency in ArAu⁺ and Related Species? *J. Am. Chem. Soc.* **1997**, *119*, 9010–9013. [CrossRef]
9. Bellert, D.; Breckenridge, W.H. Bonding in Ground-State and Excited-State A⁺·Rg van der Waals Ions (A = Atom, Rg = Rare-Gas Atom): A Model-Potential Analysis. *Chem. Rev.* **2002**, *102*, 1595–1622. [CrossRef] [PubMed]
10. Belpassi, L.; Infante, I.; Tarantelli, F.; Visscher, L.J. The Chemical Bond between Au(I) and the Noble Gases. Comparative Study of NgAuF and NgAu⁺ (Ng = Ar, Kr, Xe) by Density Functional and Coupled Cluster Methods. *Am. Chem. Soc.* **2008**, *130*, 1048–1060. [CrossRef] [PubMed]
11. Grandinetti, F. *Noble Gas Chemistry: Structure, Bonding, and Gas-Phase Chemistry*; Wiley-VCH Verlag GmbH & Co.: Weinheim, Germany, 2018.
12. Yin, B.; Luo, Z. Coinage metal clusters: From superatom chemistry to genetic materials. *Coord. Chem. Rev.* **2021**, *429*, 213643. [CrossRef]
13. Mathew, A.; Pradeep, T. Noble metal clusters: Applications in energy, environment, and biology. *Part. Part. Syst. Character.* **2014**, *31*, 1017–1053. [CrossRef]
14. Ferrari, P.; Vanbuel, J.; Janssens, P.; Lievens, P. Tuning the reactivity of small metal clusters by heteroatom doping. *Acc. Chem. Res.* **2018**, *51*, 3174–3182. [CrossRef] [PubMed]
15. de Heer, W.A. The physics of simple metal clusters: Experimental aspects and simple models. *Rev. Mod. Phys.* **1993**, *65*, 611. [CrossRef]
16. Gruene, P.; Rayner, D.M.; Redlich, B.; van der Meer, A.F.G.; Lyon, J.T.; Meijer, G.; Fielicke, A. Structures of neutral Au₇, Au₁₉, and Au₂₀ clusters in the gas phase. *Science* **2008**, *321*, 674–676. [CrossRef] [PubMed]
17. Shayeghi, A.; Heard, C.J.; Johnston, R.L.; Schäfer, R. Optical and electronic properties of mixed Ag-Au tetramer cations. *J. Chem. Phys.* **2014**, *140*, 054312. [CrossRef] [PubMed]
18. Häkkinen, H. Electronic shell structures in bare and protected metal nanoclusters. *Adv. Phys. X* **2016**, *1*, 467–491. [CrossRef]
19. Hansen, K.; Ferrari, P.; Janssens, E.; Lievens, P. Thermal radiation of gold clusters on microsecond time scales. *Phys. Rev. A* **2017**, *96*, 022511. [CrossRef]
20. Pyykko, P. Relativistic effects in structural chemistry. *Chem. Rev.* **1988**, *88*, 563–594. [CrossRef]
21. Delgado-Callico, L.; Ferrari, P.; Bakker, J.M.; Baletto, F.; Janssens, E. Benchmarking density functional theory methods for modelling cationic metal-argon complexes. *Theor. Chem. Acc.* **2021**, *140*, 38. [CrossRef]
22. Shayeghi, A.; Johnston, R.L.; Rayner, D.M.; Schäfer, R.; Fielicke, A. The nature of bonding between argon and mixed gold-silver trimers. *Angew. Chem. Int. Ed.* **2015**, *54*, 10675–10680. [CrossRef] [PubMed]
23. Shayeghi, A.; Schäfer, R.; Rayner, D.M.; Johnston, R.L.; Fielicke, A. Charge-induced dipole vs. relativistically enhanced covalent interactions in Ar-tagged Au-Ag tetramers and pentamers. *J. Chem. Phys.* **2015**, *143*, 024310. [CrossRef] [PubMed]
24. Ferrari, P.; Hou, G.-L.; Lushchikova, O.L.; Calvo, F.; Bakker, J.M.; Janssens, E. The structures of cationic gold clusters probed by far-infrared spectroscopy. *Phys. Chem. Chem. Phys.* **2020**, *22*, 11572–11577. [CrossRef]
25. Kaydashev, V.; Ferrari, P.; Heard, C.; Janssens, E.; Johnston, R.L.; Lievens, P. Optical absorption of small palladium-doped gold clusters. *Part. Part. Syst. Character.* **2016**, *33*, 364–372. [CrossRef]
26. Huang, W.; Wang, L.-S. Probing the 2D to 3D structural transition in gold cluster anions using argon tagging. *Phys. Rev. Lett.* **2009**, *102*, 153401. [CrossRef] [PubMed]

27. Goldsmith, R.; Florian, J.; Liu, J.-X.; Gruene, P.; Lyon, J.T.; Rayner, D.M.; Fielicke, A.; Scheffler, M.; Ghiringhelli, L.M. Two-to-three dimensional transition in neutral gold clusters: The crucial role of van der Waals interactions and temperature. *Phys. Rev. Mater.* **2019**, *3*, 016002. [[CrossRef](#)]
28. Lang, S.M.; Claes, P.; Cuong, N.T.; Nguyen, M.T.; Lievens, P.; Janssens, E. Copper doping of small gold cluster cations: Influence on geometric and electronic structure. *J. Chem. Phys.* **2011**, *135*, 224305. [[CrossRef](#)]
29. Kaydashev, V.E.; Janssens, E.; Lievens, P. Optical absorption spectra of palladium doped gold cluster cations. *J. Chem. Phys.* **2015**, *142*, 034310. [[CrossRef](#)] [[PubMed](#)]
30. Duncan, M.A. Invited review article: Laser vaporization cluster sources. *Rev. Sci. Instrum.* **2012**, *83*, 041101. [[CrossRef](#)]
31. Ferrari, P.; Vanbuel, J.; Li, Y.L.T.; Janssens, E.; Lievens, P. Modifications of gas aggregation sources: The double laser ablation source approach. In *Gas Aggregation Synthesis of Nanoparticles*; Wiley-VCH Verlag GmbH & Co.: Weinheim, Germany, 2017; pp. 57–78.
32. Neese, F. The ORCA quantum chemistry program package. *J. Chem. Phys.* **2020**, *152*, 224108. [[CrossRef](#)]
33. Perdew, J.P.; Burke, K.; Ernzerhof, M. Generalized gradient approximation made simple. *Phys. Rev. Lett.* **1996**, *77*, 3865. [[CrossRef](#)] [[PubMed](#)]
34. Weigend, F.; Ahlrichs, R. Balanced basis sets of split valence, triple zeta valence and quadruple zeta valence quality for H to Rn: Design and assessment of accuracy. *Phys. Chem. Chem. Phys.* **2005**, *7*, 3297–3305. [[CrossRef](#)] [[PubMed](#)]
35. Grimme, S.; Ehrlich, S.; Goerigk, L. Effect of the damping function in dispersion corrected density functional theory. *J. Comput. Chem.* **2011**, *32*, 1456–1465. [[CrossRef](#)] [[PubMed](#)]
36. Ferrari, P.; Hussein, H.A.; Heard, C.J.; Vanbuel, J.; Lievens, P.; Johnston, R.L.; Janssens, E. Effect of palladium doping on the stability and fragmentation patterns of cationic gold clusters. *Phys. Rev. A* **2018**, *97*, 052508. [[CrossRef](#)]
37. Lu, T.; Chen, F. Multiwfn: A multifunctional wavefunction analyser. *J. Comput. Chem.* **2012**, *33*, 580–592. [[CrossRef](#)]
38. Ferrari, P.; Delgado-Callico, L.; Lievens, P.; Baletto, F.; Janssens, E. Stability of cationic silver doped gold clusters and the subshell-closed electronic configuration of AgAu_{14}^+ . *J. Chem. Phys.* **2020**, *153*, 244304. [[CrossRef](#)]
39. Delgado-Callico, L.; Rossi, K.; Pinto-Miles, R.; Salzbrenner, P.; Baletto, F. A universal signature in the melting of metallic nanoparticles. *Nanoscale* **2021**, *13*, 1172–1180. [[CrossRef](#)]
40. Koumpouras, K.; Larsson, J.A. Distinguishing between chemical bonding and physical binding using electron localization function (ELF). *J. Phys. Condens. Matter.* **2020**, *32*, 315502. [[CrossRef](#)] [[PubMed](#)]